Contribution of multiple plasmon scattering in low-angle electron diffraction investigated by energy-filtered atomically resolved 4D-STEM

H. L. Robert,[1,2,3] B. Diederichs,[4,5] and K. Müller-Caspary[4,1,a)]

[1)] *Ernst Ruska-Centre for Microscopy and Spectroscopy with Electrons (ER-C), Forschungszentrum Jülich, Wilhelm-Johnen-Strasse, 52428 Jülich, Germany*

[2)] *2nd Institute of Physics, RWTH Aachen University, Templergraben 55, 52062 Aachen, Germany*

[3)] *Electron Microscopy for Materials Science (EMAT), University of Antwerp, Groenenborgerlaan 171, 2020 Antwerp, Belgium*

[4)] *Department of Chemistry, Ludwig-Maximilians-Universität München, Butenandtstrasse 5-13, 81377 Munich, Germany*

[5)] *Institute of Biological and Medical Imaging, Helmholtz Zentrum München, 85764 Neuherberg, Germany*

(Dated: 21 November 2022)

We report work on the influence of multiple plasmon-losses on the dynamical diffraction of high-energy electrons, in a scanning transmission electron microscopy (STEM) study. Using an experimental set-up enabling energy-filtered momentum-resolved STEM, it is shown that the successive excitation of up to five plasmons within the imaged material results in a subsequent and significant redistribution of low-angle intensity, in diffraction space. An empirical approach, based on the convolution with a Lorentzian kernel, is successfully tested to model this redistribution, in dependence of the energy-loss. Our study demonstrates both the significant impact of inelastic scattering in low-angle diffraction at elevated specimen thickness, and that a rather straightforward model can be applied to mimic multiple plasmon scattering, which otherwise is currently not within reach for multislice simulations, due to computational complexity.

Due to its excellent spatial resolution and the inherent capability of multidimensional characterisation, scanning transmission electron microscopy (STEM) is a key technique for the precise characterization of materials down to atomic resolution. In particular, quantitative STEM approaches based on multislice simulations[1,2], including thermal diffuse scattering[3,4], enabled the measurement of thickness, strain and chemical composition[5–7] by comparison of the experimental high-angle scattering with composition- and thickness-dependent simulations. Furthermore, the introduction of ultrafast cameras[8–12] provided access to the detailed distribution of intensity in momentum space, containing both high- and low-angle scattering. Consequently, the momentum-resolved STEM (MR-STEM) technique evolved to be a promising candidate for the comprehensive characterisation of nanostructures by exploiting the details of diffraction patterns, recorded in dependence of the probe position, over a wide range of scattering angles.

Nevertheless, early work[13] revealed a dramatic mismatch between state-of-the-art quasi-elastic simulations and experiments at scattering angles below 50 mrad. Subsequent studies[14,15] elucidated the importance of accounting for inelastic scattering, in particular due to plasmon excitations. Specifically, single plasmon scattering involves the application of a transition potential to the elastic wave function at a variety of positions in the volume of the specimen, the elastic propagation of all emerging waves down to the specimen exit face separately, and their incoherent summation[14]. It follows that multiple plasmonic excitations could be included through the application of the same scheme to each waves in a nested manner. Nevertheless, due to the resulting computational complexity, simulations are currently limited to the single plasmon excitation case. Consequently, quantifying the effect of multiple plasmon scattering on the intensity distribution, both experimentally and conceptually, suggests itself as a prerequisite for employing the wealth of information contained in the low-angle region, for quantitative materials characterisation.

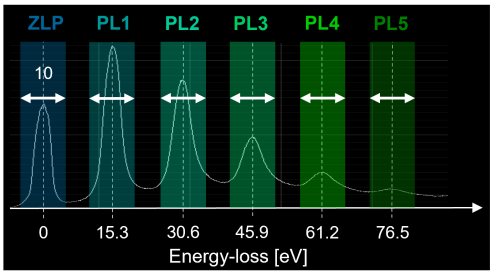

FIG. 1. Energy-loss spectrum of an Al specimen. The zero-loss peak corresponds to elastically scattered electrons, while electrons detected in the plasmon-loss peaks PL 1-5 have excited 1 to 5 plasmons while passing through the specimen. The energy windows at which MR-STEM data was recorded are indicated as well.

In this work, a dedicated MR-STEM set-up, in an aberration-corrected Hitachi HF 5000 microscope operated with an acceleration voltage $U = 200\,\mathrm{kV}$, is used to record diffraction patterns in dependence of scan position and energy-loss, at atomic spatial resolution.

[a)] k.mueller-caspary@cup.lmu.de

To this end, an ultrafast Medipix Merlin camera[9] was mounted behind a CEOS energy-filtering and imaging device (CEFID)[16]. A scan pixel size of 22 pm and a dwell time of 1 ms per scan position were used (frame rate of 1 kHz), while the semi-convergence angle was set to 20 mrad, leading to a Rayleigh resolution of approximately 76 pm. A TEM lamella of bulk Al prepared by focused ion beam milling was imaged in [100] zone axis in two different regions, denoted by A and B in the following. The local thicknesses were determined using the log-ratio approach[17,18] to (A) 74 and (B) 360 nm, respectively. For this purpose, an inelastic mean free path $\Lambda = 134$ nm was employed[19]. An example electron energy-loss (EEL) spectrum is shown in Fig. 1, where the first five plasmon peaks are clearly visible at multiples of approximately $E = 15.3$ eV energy-loss, meaning the energy transferred in a single plasmon excitation. Several MR-STEM datasets were recorded with 10 eV-wide energy windows centered on the zero-loss peak (ZLP=PL 0) and the individual plasmon peaks PL 1 to PL 5. It is noteworthy that this energy range of 10 eV was here chosen to ensure that each recording would contain only electrons having gone through the desired number of losses, and was thus limited by the achievable energy resolution. Nevertheless, as a consequence of their small width, the energy windows leave out a fraction of the respective plasmon peaks of the EEL spectrum, as is visible in Fig. 1, thus leading to some mismatches from theoretical expectations, as shown later in the text.

The effect of energy-loss on the scattered intensity is first observed in the position-averaged convergent beam electron diffraction (PACBED) patterns obtained in regions A and B, for each energy-loss separately. In the plasmon-loss case, this is justified because the excitation is delocalized in real-space. In order to visualise the effect in a compact manner, the angular dependence was calculated by averaging the PACBED intensities azimuthally as well, as shown in Fig. 2 a for dataset A. Elliptical distortions at the level of the detector were accounted for by distorting the two-dimensional angular scaling accordingly[20,21]. It is noteworthy that such a polar integration forms the basis for angle-resolved STEM (AR-STEM), which is the method that initially revealed the importance of inelastic scattering when employing annular detectors[13,22]. By convention, the data is normalized to the incident intensity I_0 and to solid angle.

It is instructive to analyse the trend of the angular dependences in Fig. 2 a with increasing energy-loss. Within the Ronchigram, below 20 mrad, intensity remains almost constant and is separated from the dark field via a step-like drop. This step is sharpest for elastically scattered electrons contained in the ZLP, and consecutively smears out with an increasing number of excited plasmons. In particular, the Ronchigram border is barely visible in the log-scale plot after five plasmon excitations. The ratios of successive angular dependences are plotted in Fig. 2 b, showing explicitly that each energy-loss obeys its own angular behaviour, such that multiple plasmon scattering can have a significant impact in AR-STEM if the specimen thickness is large enough to yield significant intensity in the respective plasmon peaks.

Moreover, the PACBED patterns in Fig. 2 c obtained for the different energy-losses suffer from a strong blurring of sharp features present in the elastic ZLP data, which is amplified at each energy-loss. Finally, the loss-

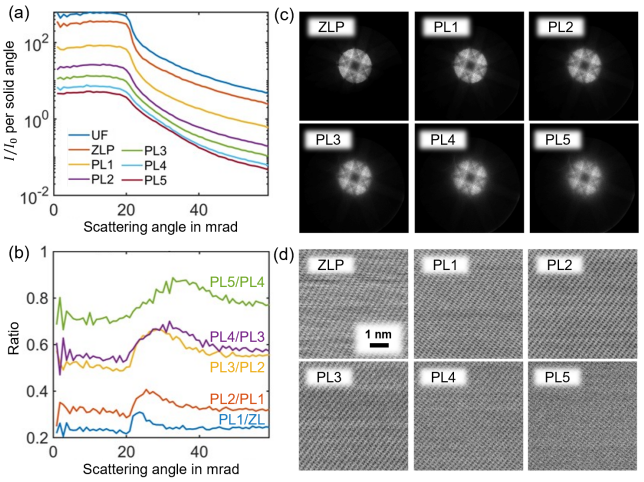

FIG. 2. Results of the energy-filtered MR-STEM experiments performed in region A with a thickness of 74 nm. (a) Position- and azimuthally averaged angular dependences of scattered intensity, per Sr and normalized to I_0, for the unfiltered (UF) case, zero-loss-peak (ZLP) and up to five plasmon excitations (PL 1-5). (b) Angle-dependent ratio of successive inelastic intensities from (a). (c) PACBED patterns. (d) BF images.

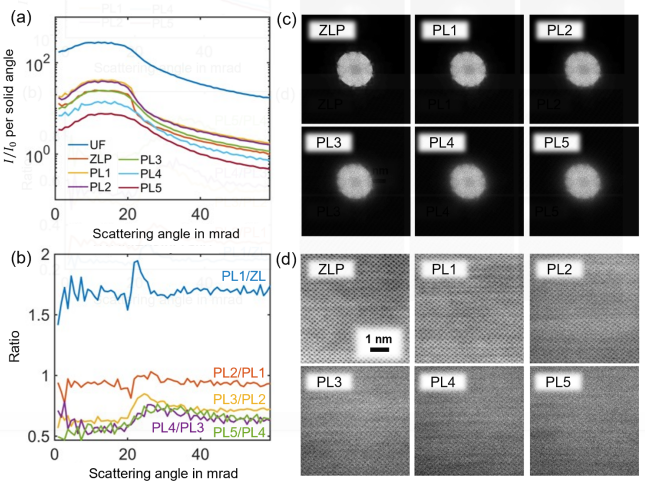

FIG. 3. Results of the energy-filtered MR-STEM experiments performed in region B with a thickness of 360 nm. (a) Position- and azimuthally averaged angular dependences of scattered intensity, per Sr and normalized to I_0, for the unfiltered (UF) case, zero-loss-peak (ZLP) and up to five plasmon excitations (PL 1-5). (b) Angle-dependent ratio of successive inelastic intensities from (a). (c) PACBED patterns. (d) BF images.

dependent bright field (BF) STEM images in Fig. 2 d are obtained by summing all detected electrons within the primary beam. Although decreasing, elastic contrast and atomic resolution are preserved in real-space[23,24] with an increasing number of plasmon excitations. Indeed, the co-occurrence of elastic and inelastic scattering ensures that, within an electron wave having lost energy at a certain point of its propagation through the specimen, interference of the Bragg beams still occurs in the far-field. In the present study, the atomic-resolution BF data confirms the stability of the instrument throughout the recordings making up the five-dimensional dataset.

The results obtained in the approximately five times thicker region B are given in Fig. 3. Qualitatively, the same arguments hold as to the subsequent angular broadenings. It should be noted that inelastic scattering involving one to four plasmon excitations exceeds the elastically scattered number of electrons, as seen in Fig. 3 a. Whereas such elevated thicknesses are beyond common STEM applications on the one hand, they are still used in quantitative convergent-beam electron diffraction on the other hand, where the alleviation of inelastic scattering effects is often required[25]. Here, the thicknesses of 74 and 360 nm respectively serve as common and extreme cases to check the reliability of the empirical description of the momentum transfer associated with plasmon-losses, as presented in the following.

In that respect, a reminder of the implications of the ratios in Figs. 2 and 3 b is relevant. If inelastic scattering had not changed the angular dependence of the scattered intensity, the ratio would be constant, that is, solely the energy of the electrons would change, without any momentum transfer. For single plasmon excitations, earlier work[14,22,26] utilised the convolution of simulated diffraction patterns with a kernel derived from a transition potential as an approximation to an explicit inelastic simulation including dynamical scattering. It is interesting to note that such an approximation can be understood as a result of imposing the commutativity of the propagation operator and the transition potential, within the multislice model[14], which, in practice, leads to an omission of the co-occurrence of propagation effects and energy-loss, in the description. Here, a Lorentzian kernel $L_1(\vec{q})$ according to the dipole approximation[27] is used,

$$L_1\left(\vec{q}\right) = p_1 \left(\frac{L_0}{q^2 + q_E^2}\right) \quad , \tag{1}$$

where p_1 represents the proportion of incident electrons having excited a plasmon during the propagation and q_E is a spatial frequency characteristic of the energy-loss. In the present case, a theoretical value $q_E \approx 0.0153\,\mathrm{nm}^{-1}$ can be obtained from[27]

$$q_E = \frac{1}{\lambda} sin\left(\frac{E}{2eU}\right) \tag{2}$$

with λ the electron wavelength and e the elementary charge. The dipolar approximation is typically valid up

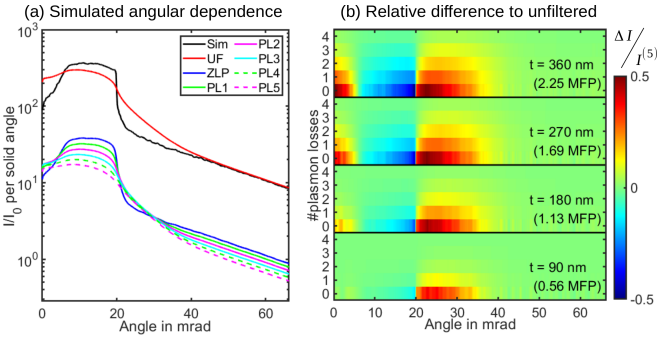

FIG. 4. a) Simulated angular dependence for 360 nm specimen thickness in dependence of the energy-loss, based on a frozen phonon multislice result. Lorentzian parameters were $q_E = 0.015\,\mathrm{nm}^{-1}$ with a cutoff at 15 mrad. b) Simulated relative error when 0 to 5 plasmons are included in dependence of scattering angle and specimen thickness. The case with 5 plasmon excitations included is considered as unfiltered.

to angles between 10 and 20 mrad, where it is cut off. L_0 thus serves to numerically normalise the 2D Lorentzian, once this cut-off has been done. Assuming that the diffraction pattern for a single plasmon-loss can be derived from a quasi-elastic simulation $I_{FP}(\vec{q})$ employing the frozen phonon multislice approach, it is given by

$$I_{\mathrm{PL}}^{(1)}(\vec{q}) = I_{\mathrm{FP}}(\vec{q}) \otimes L_1(\vec{q}) \tag{3}$$

and the zero-loss pattern is obtained by

$$I_{\mathrm{ZL}}(\vec{q}) = (1 - p_1) \cdot I_{\mathrm{FP}}(\vec{q}) \quad , \tag{4}$$

being the original simulation with the first plasmon-loss intensity removed. To account for multiple plasmon scattering and obtain $I_{\mathrm{PL}}^{(n)}(\vec{q})$, eq. (3) must be applied recursively by convolving $I_{\mathrm{PL}}^{(n-1)}(\vec{q})$ with a kernel $L_{(n)}(\vec{q})$. It is reasonable to assume $L_{(n)}(\vec{q}) = L_1(\vec{q})$ since each plasmon scattering event obeys the same underlying physics. By using the Fourier convolution theorem, the dependence of scattered intensity after n plasmon-losses is straightforwardly obtained from a simulation $I_{\mathrm{FP}}(\vec{q})$ via

$$I_{\mathrm{PL}}^{(n)}(\vec{q}) = \mathcal{F}^{-1}\left[\mathcal{F}\left[I_{\mathrm{FP}}(\vec{q})\right](\vec{r}) \left(\tilde{L}_1(r)\right)^n\right](\vec{q}) \tag{5}$$

with $\tilde{L}_1(r)$ the inverse Fourier transform of $L_1(\vec{q})$. This indicates a decay of the plasmon scattering according to p_1^n, for which $p_1 = 1 - \mathrm{e}^{-\frac{t}{\Lambda_P}}$ has proven applicable. Λ_P is here the mean free path for plasmon scattering, and t the specimen thickness. For bulk Al, a value of $\Lambda_P = 160\,\mathrm{nm}$ can be employed[19], leading to $p_1 \approx 0.37$ for region A and $p_1 \approx 0.89$ for region B.

Multiple plasmon scattering is dominant in region B, which makes it a suitable example to study to which extent a quasi-elastic frozen phonon multislice PACBED simulation for 360 nm-thick Al [100], in combination with eq. (5), can represent the experimentally observed angular broadening. The black curve in Fig. 4 a represents

the azimuthal intensity per Sr of the native simulation, of which only 11 % remain in the elastic signal (ZLP) shown in blue. Azimuthal intensities for up to five subsequent plasmon excitations, with $q_E = 0.015\,\mathrm{nm}^{-1}$ (corresponding to 5 pixels in the simulation), are depicted too, showing an exponential decay of intensity with the number of plasmons according to p_1^n. Furthermore, a strong angular broadening affects the Ronchigram edge at 20 mrad. By summing up the elastic (ZLP) signal and all plasmon-losses, the red curve is obtained, which can be interpreted as a simulated unfiltered (UF) angular dependence. Note that both features and magnitudes of the simulations based on the convolutional approach fit the experimental counterpart in Fig. 3 a rather well. Differences in the scaling of the individual plasmon contributions are expected due to the small width of the energy windows, as mentioned previously.

The dependence of the plasmon-loss-induced angular broadening on specimen thickness suggests an analysis of the number of excitations that need to be considered at a given thickness, which is presented in Fig. 4 b. For thicknesses between 90 and 360 nm, the azimuthal sums have been calculated as in figure part a), though by taking a maximum of $0 \ldots 4$ plasmon-losses into account to calculate the unfiltered result. Then, the difference ΔI to a simulation $I^{(5)}$ including five plasmon excitations was calculated, which, for the material and thickness range dealt with here, can be regarded as converged owing to Fig. 1. Fig. 4 b depicts the relative error $\Delta I / I^{(5)}$ in dependence of scattering angle, specimen thickness and number of losses included. Whereas the neglect of plasmon excitations leads to errors of up to 50 % in all cases, taking only the broadening due to a single excitation into account is already sufficient for 90 nm thick specimen. For a thickness of 180 nm, the error becomes low if two plasmon-losses are taken into account. At even higher thicknesses, including three excitations appears sufficient. Of course, these conclusions depend on the characteristic spatial frequency q_E and the plasmon-loss mean free path Λ_P. However, the former does not vary strongly among materials, such that the thicknesses in terms of Λ_P in Fig. 4 b should provide a general guide for the number of plasmons to consider in an AR-STEM experiment, for a wide range of materials.

Furthermore, the experimental results presented in Fig. 2,3 can be exploited directly in an empirical verification of the applicability of a Lorentzian function to represent the redistribution of intensity due to inelastic scattering. There, the experimental PACBED patterns can be identified to $I_{PL}^{(n)\,;\,exp}(\vec{q}) = (1-\alpha_{(n)})(1-p_1) I_{PL}^{(n)}(\vec{q})$, where $(1-p_1)$ expresses the attenuation due to the excitation of the $(n+1)$-th plasmon and $\alpha_{(n)}$ is the proportion of electrons lost in the recording of $I_{PL}^{(n)\,;\,exp}$, due to the small width of the energy window. The successively recorded intensities are thus expected to satisfy

$$\frac{I_{PL}^{(n-1)\,;\,exp}(\vec{q}) \otimes L_{(1)}(\vec{q})}{(1-\alpha_{(n-1)})} - \frac{I_{PL}^{(n)\,;\,exp}(\vec{q})}{(1-\alpha_{(n)})} = 0 \qquad (6)$$

where $I_{PL}^{(0)\,;\,exp}(\vec{q}) = I_{ZL}^{exp}(\vec{q})$. Eq. (6) can then be used to directly fit a parametric Lorentzian $\beta_{(n)} L_{(1)}(\vec{q})$, where $\beta_{(n)} = \frac{1-\alpha_{(n)}}{1-\alpha_{(n-1)}}$, to the experimental data, by minimizing the error function

$$\epsilon = \sum_{\vec{q}} \mid I_{PL}^{(n)\,;\,exp}(\vec{q}) - I_{PL}^{(n-1)\,;\,exp}(\vec{q}) \otimes \left(\beta_{(n)} L_{(1)}(\vec{q})\right) \mid^2 \quad , \qquad (7)$$

while adjusting q_E, in accordance to eq. (1), and $\beta_{(n)}$[28]. In that way, a common value for the parameter q_E is found for all excitations in both regions, with correction of the $\beta_{(n)}$ factors. L_0 is again employed to normalize the Lorentzian function, which is cut off at 15 mrad. Though the convolution is performed in the two-dimensional reciprocal space, ϵ is calculated by comparison of the one-dimensional angular dependences, in order to remove the influence of possible rotation and shift effects of the diffraction patterns, occurring from one window to the next. Values extracted for q_E are $0.0221\,\mathrm{nm}^{-1}$ in region A and $0.0214\,\mathrm{nm}^{-1}$ in region B, the fit being concluded with an average relative error of (A) 3.92 % and (B) 6.38 %. The empirically determined characteristic scattering angles are thus slightly higher than the theoretical value of $0.0153\,\mathrm{nm}^{-1}$, though remaining very close to it. Mismatches can be explained by the finite sampling of diffraction space by the pixels of the camera, each of them covering a surface of about $(0.18\,\mathrm{nm}^{-1})^2$, thus close to ten times q_E^2. It is noteworthy that the quality of fit is generally higher for the region A data, which can be related to the greater intensity of the corresponding diffraction patterns, which is in turn due to the lower thickness traveled by the electrons, ensuring that a lower proportion of those are scattered beyond the camera range.

With this conclusive verification, and the simulation results presented in Fig. 4, the validity of an approach based on the convolution with a Lorentzian function, to account for inelastic scattering in quantitative MR-STEM, is demonstrated. Such a finding has important implications in two respects. First, it shows that, even if an inelastic scattering event occurs within a 3D volume, and is thus followed by a subsequent elastic dynamical diffraction by the crystalline specimen, the assumption of commutativity in the multislice description remains reasonable in practice. Second, provided that this convolutional model is employable in simulations, the inherent computational complexity of the scattering phenomena observed here may be alleviated. Such a possibility could thus lead to important progresses in quantitative STEM, in particular with the description of low-angle scattering in MR-STEM, which has been shown to be rich in, e.g, information relating to chemical composition[13].

ACKNOWLEDGMENTS

This work was supported by the Initiative and Network Fund of the Helmholtz Association (Germany) under contracts VH-NG-1317 and ZT-I-0025.

[1] J. M. Cowley and A. F. Moodie, "The scattering of electrons by atoms and crystals. I. A new theoretical approach," Acta Crystallographica **10**, 609–619 (1957).

[2] D. F. Lynch and M. A. O'Keefe, "n-Beam lattice images. II. Methods of calculation," Acta Crystallographica Section A **28**, 536–548 (1972).

[3] J. M. LeBeau and S. Stemmer, "Experimental quantification of annular dark-field images in scanning transmission electron microscopy," Ultramicroscopy **108**, 1653–1658 (2008).

[4] A. Rosenauer, M. Schowalter, J. T. Titantah, and D. Lamoen, "An emission-potential multislice approximation to simulate thermal diffuse scattering in high-resolution transmission electron microscopy," Ultramicroscopy **108**, 1504–1513 (2008).

[5] A. Rosenauer, K. Gries, K. Müller, A. Pretorius, M. Schowalter, A. Avramescu, K. Engl, and S. Lutgen, "Measurement of specimen thickness and composition in Alx Ga1 - x N / GaN using high-angle annular dark field images," Ultramicroscopy **109**, 1171–1182 (2009).

[6] A. Rosenauer, T. Mehrtens, K. Müller, K. Gries, M. Schowalter, P. Venkata Satyam, S. Bley, C. Tessarek, D. Hommel, K. Sebald, M. Seyfried, J. Gutowski, A. Avramescu, K. Engl, S. Lutgen, P. V. Satyam, S. Bley, C. Tessarek, D. Hommel, K. Sebald, M. Seyfried, J. Gutowski, A. Avramescu, K. Engl, and S. Lutgen, "Composition mapping in InGaN by scanning transmission electron microscopy," Ultramicroscopy **111**, 1316–1327 (2011).

[7] T. Grieb, K. Müller, O. Rubel, R. Fritz, C. Gloistein, N. Neugebohrn, M. Schowalter, K. Volz, and A. Rosenauer, "Determination of the chemical composition of GaNAs using STEM HAADF imaging and STEM strain state analysis," Ultramicroscopy **117**, 15–23 (2012).

[8] K. Müller, H. Ryll, I. Ordavo, S. Ihle, L. Strüder, K. Volz, J. Zweck, H. Soltau, and A. Rosenauer, "Scanning transmission electron microscopy strain measurement from millisecond frames of a direct electron charge coupled device," Appl. Phys. Lett. **101**, 212110 (2012).

[9] R. Plackett, I. Horswell, E. N. Gimenez, J. Marchal, D. Omar, and N. Tartoni, "Merlin: a fast versatile readout system for Medipix3," Journal of Instrumentation **8**, C01038 (2013).

[10] K. Müller-Caspary, A. Oelsner, and P. Potapov, "Two-dimensional strain mapping in semiconductors by nano-beam electron diffraction employing a delay-line detector," Appl. Phys. Lett. **107**, 72110 (2015).

[11] H. Ryll, M. Simson, R. Hartmann, P. Holl, M. Huth, S. Ihle, Y. Kondo, P. Kotula, A. Liebel, K. Müller-Caspary, A. Rosenauer, R. Sagawa, J. Schmidt, H. Soltau, and L. Strüder, "A pnCCD-based, fast direct single electron imaging camera for TEM and STEM," J. Instrum. **11**, P04006 (2016).

[12] M. W. Tate, P. Purohit, D. Chamberlain, K. X. Nguyen, R. Hovden, C. S. Chang, P. Deb, E. Turgut, J. T. Heron, D. G. Schlom, D. C. Ralph, G. D. Fuchs, K. S. Shanks, H. T. Philipp, D. A. Muller, and S. M. Gruner, "High Dynamic Range Pixel Array Detector for Scanning Transmission Electron Microscopy," Microsc. Microanal. **22**, 237–249 (2016), arXiv:1511.03539.

[13] K. Müller-Caspary, O. Oppermann, T. Grieb, F. F. Krause, A. Rosenauer, M. Schowalter, T. Mehrtens, A. Beyer, K. Volz, and P. Potapov, "Materials characterisation by angle-resolved scanning transmission electron microscopy," Scientific Reports **6**, 1–9 (2016).

[14] A. Beyer, F. F. Krause, H. L. Robert, S. Firoozabadi, T. Grieb, P. Kükelhan, D. Heimes, M. Schowalter, K. Müller-Caspary, A. Rosenauer, and K. Volz, "Influence of plasmon excitations on atomic-resolution quantitative 4D scanning transmission electron microscopy," Scientific Reports **10**, 17890 (2020).

[15] J. Barthel, M. Cattaneo, B. G. Mendis, S. D. Findlay, and L. J. Allen, "Angular dependence of fast-electron scattering from materials," Physical Review B **101**, 1–9 (2020).

[16] F. Kahl, V. Gerheim, M. Linck, H. Müller, R. Schillinger, and S. Uhlemann, "Test and characterization of a new post-column imaging energy filter," in *Advances in Imaging and Electron Physics*, Vol. 212 (Elsevier Inc., 2019) pp. 35–70.

[17] R. D. Leapman, C. E. Fiori, and C. R. Swyt, "Mass thickness determination by electron energy loss for quantitative X-ray microanalysis in biology," Journal of Microscopy **133**, 239–253 (1984).

[18] T. Malis, S. C. Cheng, and R. F. Egerton, "EELS log-ratio technique for specimen-thickness measurement in the TEM," Journal of Electron Microscopy Technique **8**, 193–200 (1988).

[19] K. Iakoubovskii, K. Mitsuishi, Y. Nakayama, and K. Furuya, "Mean free path of inelastic electron scattering in elemental solids and oxides using transmission electron microscopy: Atomic number dependent oscillatory behavior," Physical Review B - Condensed Matter and Materials Physics **77**, 1–7 (2008).

[20] K. Müller, A. Rosenauer, M. Schowalter, J. Zweck, R. Fritz, and K. Volz, "Strain measurement in semiconductor heterostructures by scanning transmission electron microscopy," Microsc. Microanal. **18**, 995–1009 (2012).

[21] H. L. Robert, I. Lobato, F. Lyu, Q. Chen, S. Van Aert, D. Van Dyck, and K. Müller-Caspary, "Dynamical diffraction of high-energy electrons investigated by focal series momentum-resolved scanning transmission electron microscopy at atomic resolution," Ultramicroscopy **233**, 113425 (2021).

[22] T. Grieb, F. F. Krause, K. Müller-Caspary, S. Firoozabadi, C. Mahr, M. Schowalter, A. Beyer, O. Oppermann, K. Volz, and A. Rosenauer, "Angle-resolved STEM using an iris aperture: Scattering contributions and sources of error for the quantitative analysis in Si," Ultramicroscopy **221**, 113175 (2021).

[23] H. Kohl, "Image formation by inelastically scattered electrons: Image of a surface plasmon," Ultramicroscopy **11**, 53–65 (1983).

[24] H. Kohl and H. Rose, *Advances in Electronics and Electron Physics*, Vol. 65 (1985) pp. 173–227.

[25] M. Tanaka, K. Tsuda, M. Terauchi, K. Tsuno, T. Kaneyama, T. Honda, and M. Ishida, "A new 200 kV Ω-filter electron microscope," Journal of Microscopy **194**, 219–227 (1999).

[26] T. Grieb, F. F. Krause, C. Mahr, D. Zillmann, K. Müller-Caspary, M. Schowalter, and A. Rosenauer, "Optimization of {NBED} simulations for disc-detection measurements," Ultramicroscopy **181**, 50–60 (2017).

[27] R. F. Egerton and K. Wong, "Some practical consequences of the Lorentzian angular distribution of inelastic scattering," Ultramicroscopy **59**, 169–180 (1995).

[28] J. C. Lagarias, J. A. Reeds, M. H. Wright, and P. E. Wright, "Convergence properties of the Nelder-Mead simplex method in low dimensions," SIAM Journal on Optimization **9**, 112–147 (1998).